ACS OMEGA

http://pubs.acs.org/journal/acsodf

Article

Asymmetrical Electrical Performance across Different Planes of Solution-Grown $MAPbBr_3$ Crystals of mm Dimensions

Kunchanapalli Ramya, Arindam Mondal, Dr. Satyajit Gupta,* and Dr. Sabyasachi Mukhopadhyay*

Cite This: *ACS Omega* 2022, 7, 42138−42145

Read Online

ACCESS | Metrics & More | Article Recommendations | Supporting Information

ABSTRACT: Throughout a few years, carrier transport studies across HaP single crystals have gained enormous importance for current generation photovoltaic and photodetector research with their superior optoelectronic properties compared to commercially available polycrystalline materials. Utilizing the room-temperature solution-grown method, we synthesized $MAPbBr_3$ crystals and examined their electrical transport properties. Although the X-ray diffraction reveals the cubical nature of the crystals, we have observed anisotropy in the electrical transport behavior and variation in dielectric constant across the three opposite faces of the crystals of mm dimensions. The face with a higher dielectric constant depicts improved parameters from electrical characteristics such as lower trap densities and higher mobility values. We further explore the origin of its anisotropic nature by performing X-ray diffraction on three opposite faces of crystals. Our studies define the specific faces of cuboid-shaped $MAPbBr_3$ crystals for efficient electrical contact in the fabrication of optoelectronic devices.

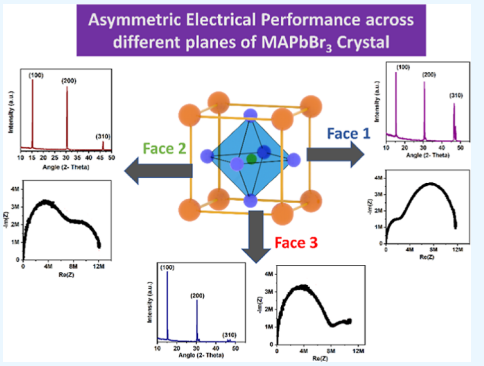

INTRODUCTION

Lead halide perovskites have been widely used in solar cells and photodetectors and play a significant role in the semiconductor industry with 25.7% of power conversion efficiency.[1−6] Polycrystalline halide perovskite materials used in most optoelectronic applications are generally fabricated by drop-casting or spin-coating techniques. They possess a high density of defects, especially at grain boundaries, thus reducing the performance of carrier mobility across the crystals.[7−9] In that respect, lead halide perovskite single crystals with lower grain boundaries and carrier recombination have become more promising in optoelectronic applications, as demonstrated in recent studies.[10] Various methods have been used to synthesize halide perovskite materials, including the inverse temperature crystallization method, crystallization by the anti-solvent vapor-assisted way, and the traditional high-temperature Bridgman method.[11−17] Trap density and carrier mobility are among the main factors that hinder the efficiency in device applications of organic halide perovskites. Thus, there is a requirement to synthesize more straightforward and cost-effective halide perovskite crystals with lower trap density and high carrier mobilities. Instead of expensive precursor salts and toxic solvents, we synthesized $MAPbBr_3$ crystals using *N*-methyl formamide (NMF) as a solvent that contributes to methylammonium ions (MA = $CH_3NH_3^+$) at room temperature.[18]

Structural properties of the crystals, such as crystal plane orientation and grain boundaries, could play a crucial role in device performance made of perovskite crystals. For example, in the case of crystals, the electrical parameters such as trap density and carrier mobilities alter with various crystal plane directions, impacting electrical transport performance and charge carriers' injection/extraction efficiencies.[13,19−25] In XRD methods, performed on three faces of the crystals, we have obtained the presence of various crystal plane orientations on three opposite faces of our synthesized perovskite crystals. We have explored the electrical characteristics of synthesized perovskite crystals across their different faces to investigate the crystal structure effect on electronic transport. In this work, we have studied how the structural arrangement of perovskite crystals affects their electrical characteristics across the various opposite faces, which leads to efficient electrical contact in the device fabrication. In addition, we have explored the effect of grain boundaries on the electrical properties by studying the electrical characteristics across powdered crystals in the pellet form and comparing them with the electrical properties along with various opposite faces of the mm dimension $MAPbBr_3$ crystals.

EXPERIMENTAL SECTION

Synthesis Methods of $MAPbBr_3$ Single Crystals and Pellets Made out of Powdered Crystals. A low-temper-

Received: July 25, 2022
Accepted: October 13, 2022
Published: November 9, 2022

ature solution-grown synthesis method was used to prepare $MAPbBr_3$ crystals, and the detailed procedure is discussed in the previous literature.[18] In brief, $PbBr_2$ was dissolved in NMF containing HBr by sonication and vortexing (Figure S1). It was then left in the dark for 48 h to obtain the mm dimension bulk $MAPbBr_3$ crystals.[10]

The bulk crystals were powdered using the ball mill method by grinding the crystals into finite powder of micro−nano crystal dimensions. Then, an adequate amount of powder was pressed using a hydraulic press to make the pellet. Finally, pellets with a diameter of 8 mm were made and kept for thermal annealing at 200 °C in a vacuum to obtain the structural stability of the pellet.

Structural Characterization. Previous studies have examined and reported the structural properties of $MAPbBr_3$ crystals in powder form.[10] The XRD analysis of the crystal has been performed on the different faces of $MAPbBr_3$ crystals using a Bruker D8 Advance, Cu−K(alpha) X-ray diffractometer with X-rays of wavelength 1.54 Å and analyzed using Rietveld refinement and peak fittings.

Electrical Measurements:

The electrical measurements across the various faces of the crystals and pellets were performed using the Keithley source measurement unit 2636B series with a 0−20 dc applied bias range. The electrical properties of the crystal faces and the pellets were performed by coating with the silver metal paste on opposite surfaces of crystals and pellets (Figure 1). The

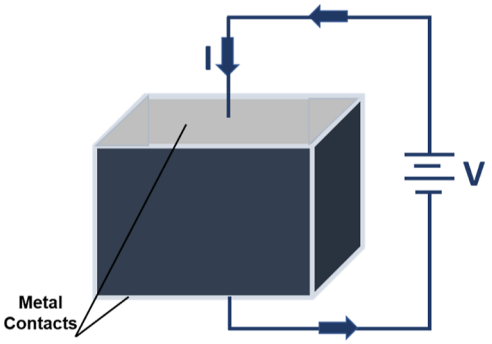

Figure 1. Schematic electrical measurements across the different opposite faces of the $MAPbBr_3$ crystals and pellets.

current across opposite faces of a crystal was measured with the applied bias range from 0 V to 20 V. In addition, the current−voltage characteristics were analyzed following the space charge limited current (SCLC) method. As a result, electrical parameters such as trap density and carrier mobilities were obtained, affecting the device efficiency of the crystals for optoelectronic applications.

Dielectric Measurements. The dielectric measurements of $MAPbBr_3$ crystals across various faces and the pellet made from the powdered crystals were performed by impedance spectroscopy.[26] A silver paint layer was applied on the opposite faces of crystals, and pellets of $MAPbBr_3$ crystals served as an electrical contact in dielectric measurements. The voltage at the probe impedes the dielectric layer across the metal contacts (Figure 1). Measurements were carried out with an impedance analyzer (Wayne Kerr Inc. 6500B series of 20 Hz to 10 MHz frequency range) under both dark and green illumination [using green light-emitting diode (LED) $\lambda \sim 560$ nm] conditions.

RESULTS AND DISCUSSION

We have illustrated a schematic of $MAPbBr_3$ crystals in a cubic structure in Figure 2a. The corner atoms represent bromine ions, and the central green part represents the MA ions. Optical images of solution-grown $MAPbBr_3$ crystals at our laboratory with their relative dimensions are shown in Figure 2b. Our analysis has defined a specific $MAPbBr_3$ crystal (Figure 2c) with a side length of 4 mm as face I, 3 mm as face II, and 2 mm as face III.

Dielectric Properties. Our experiments considered cuboid geometrical shaped $MAPbBr_3$ crystals of different faces with various surface dimensional areas. The dielectric studies of $MAPbBr_3$ crystals across opposite faces were performed using an impedance spectroscopy tool, where resistance and reactance, known as real and imaginary parts of the impedance, with applied ac voltages (ranging from 10−500 mV non-uniformly) were measured. These dielectric measurements were performed for the crystals across the opposite faces under dark and green LED illumination conditions (wavelength ∼ 560 nm). Intrinsic carrier concentrations consisting of electrons, holes, and free ions within the crystals under dark conditions participate in electronic transport.[26] Under green illumination, more photogenerated carriers are incorporated in electronic transport with various applied biases. Figure 3a−c represent the Nyquist plot of impedance measurements across three opposite faces of cuboidal-shaped $MAPbBr_3$ crystals. We expected near-symmetric dielectric behavior from cubic crystals along the three opposite surfaces. However, for most of our synthesized $MAPbBr_3$ crystals (with dimensions between 2 and 4 mm), we have observed different dielectric behaviors across various faces of the crystals, which we further investigated and discussed. Some of the opposite surfaces of $MAPbBr_3$ crystals showed similar impedance behavior as the

Figure 2. (a) Schematic of the cubic $MAPbBr_3$ structure; the central green region represents the MA cation, and the blue dots represent the Br atoms (b) One of the synthesized $MAPbBr_3$ crystals. (c) Dimension of the specific $MAPbBr_3$ crystal considered in our analysis.

https://doi.org/10.1021/acsomega.2c04681
ACS Omega 2022, 7, 42138−42145

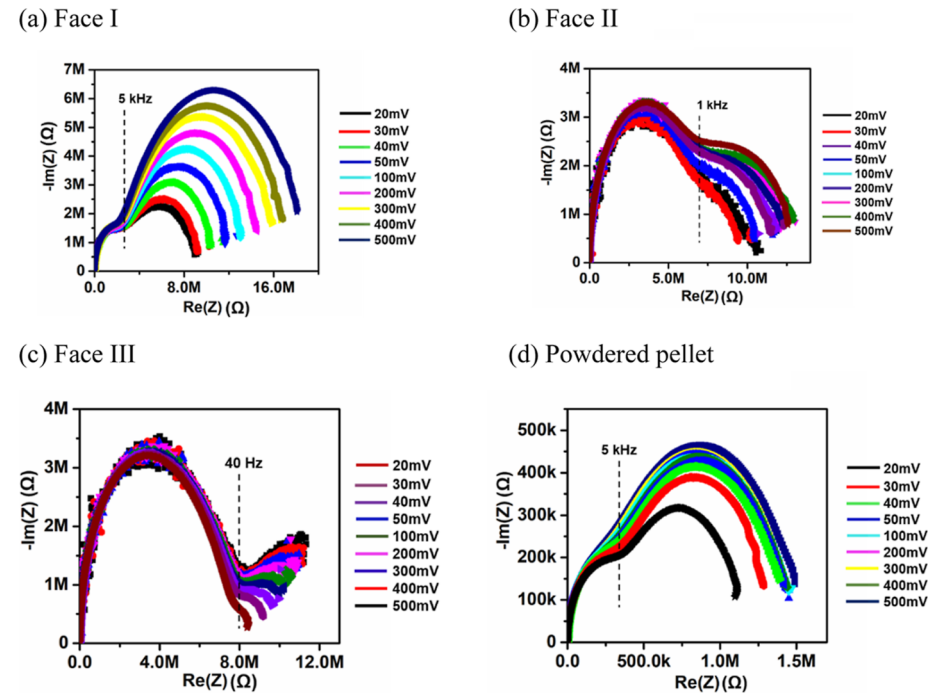

Figure 3. Representation of the Nyquist plot of impedance measurements under dark for three different opposite surfaces of $MAPbBr_3$ crystals (a–c) and in a pellet form (d)[10] (Reprinted with permission from ref 10 with license number 5351940481677. Copyright 2022 Elsevier).

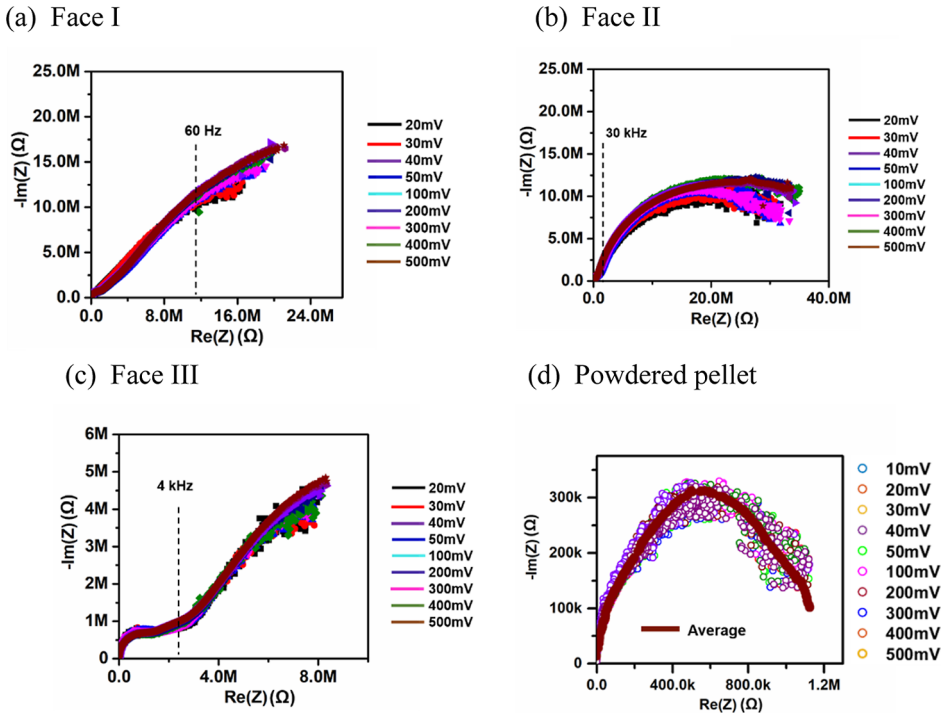

Figure 4. Representation of the Nyquist plot of impedance measurements under green illumination conditions for three different opposite surfaces of $MAPbBr_3$ crystals (a–c) and in pellet form (d)[10] (Reprinted with permission from ref 10 with license number 5351940481677. Copyright 2022 Elsevier).

one we obtained in our earlier studies across the perovskite in the pellet form (Figure 3d) under various applied ac biases.[10]

Nyquist plots from our impedance measurements across various opposite faces of $MAPbBr_3$ crystals depict two semi-circles represented by two resistance-capacitor (RC) parallel components in equivalent circuits. The semi-circle at the high-frequency regime reveals low resistance values for electronic transport, and ionic transport is represented by the semi-circle with higher resistance values at the lower frequency regime. We have designated three opposite faces of one of the $MAPbBr_3$ crystals in three faces, as represented in Figure 1. For face I (Figure 3a), low-frequency semi-circles (in the range of 20 Hz to 5.8 kHz) are more prominent, and the change in applied ac voltages reflects ion accumulation at electronic

https://doi.org/10.1021/acsomega.2c04681
ACS Omega 2022, 7, 42138−42145

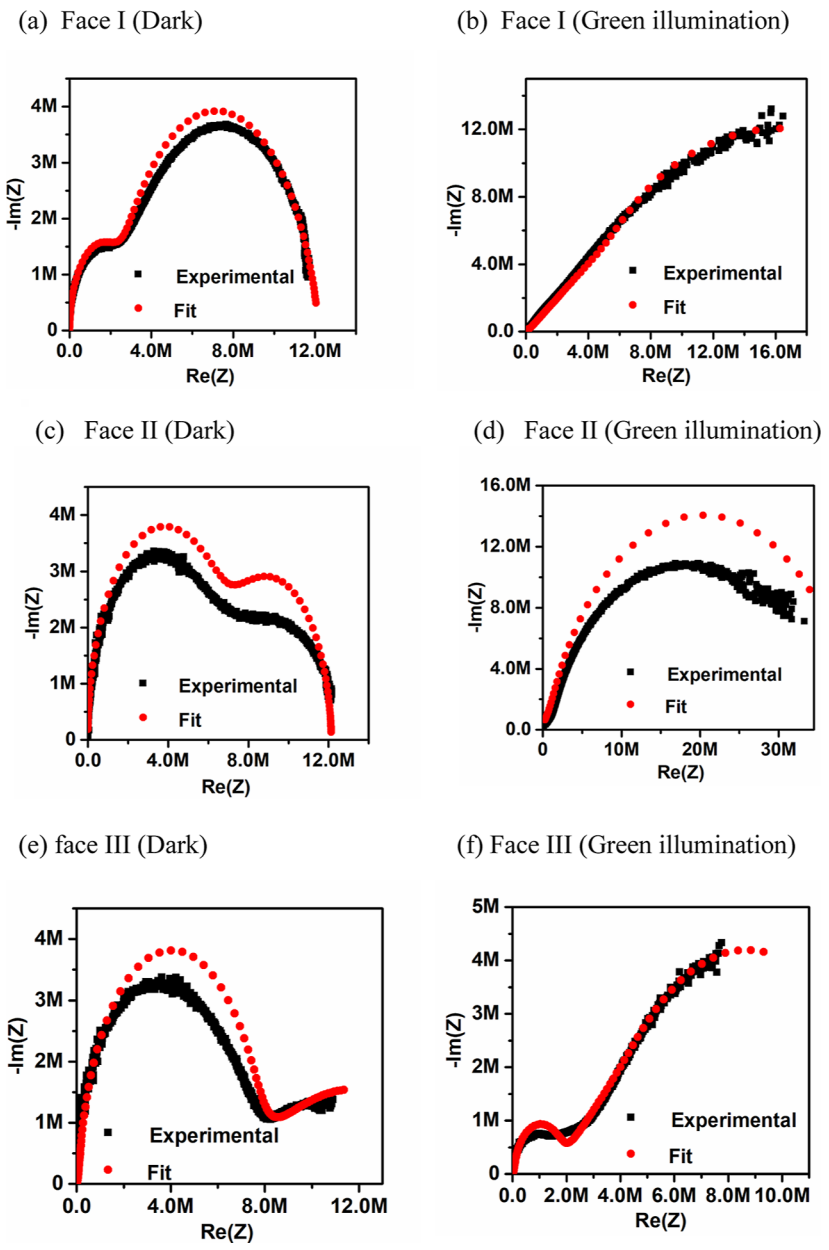

Figure 5. Impedance spectra of the equivalent electrical circuit and the corresponding experimental data obtained under dark and green illumination conditions with a 50 mV AC bias.

contact interfaces. It reveals that the ionic transport is more dominant in face I of $MAPbBr_3$ crystals than electronic transport. In the second case of face II of the crystals (Figure 3b), semi-circles at higher (in the range of 1.85 kHz to 10 MHz) and lower frequency regimes (in the range of 20 Hz to 1.85 kHz) are distinct. They represent electronic and ionic transport contributions across the opposite faces of crystals. Only a dominant semi-circle at a high-frequency regime (in the range of 3.58 kHz to 10 MHz) was obtained for face III, compared to the ionic contribution at low frequency (Figure 3c), concluding efficient electronic transport across the opposite faces of the crystals. We also observed a reduction of calculated peak resistance (8−10 MΩ) for face III with various ac applied voltages compared to (10−12 MΩ) face II and 16 MΩ in face I.

Nyquist plot for the pellets of $MAPbBr_3$ in the form of pellet is represented in Figure 3d (Reprinted with permission from ref 10 with license number 5351940481677. Copyright 2022 Elsevier) with various ac applied voltages.[10] Even though the two semi-circles were distinct, ionic transport is dominated in the low-frequency regime (in the range of 20 Hz to 4.98 kHz).[26] Thus, our experimental observations support the altered dielectric behavior of synthesized $MAPbBr_3$ crystals when measured across various opposite faces and the pellet form of the powdered crystals.[27]

Upon green illuminations, face I depicts a saturation of ionic carrier transport at a low-frequency regime (range of 20 Hz to 59 Hz), showing a straight line at 45°, representing the "Warburg element" in the equivalent circuit (Figure 4a).[27] We have discussed the origin of the "Warburg element" and its physical significance in the next section. The semi-circle at the high-frequency regime follows the low-frequency "Warburg element." Across face II, a single semi-circle in Nyquist plots represents nothing but a single RC circuit and a combined

https://doi.org/10.1021/acsomega.2c04681
ACS Omega 2022, 7, 42138−42145

electronic and ionic transport contribution. For face III of $MAPbBr_3$ crystals under green illumination, high-frequency (in the range of 3.58 kHz to 10 MHz) semi-circle and low-frequency (20 Hz to 2.58 kHz) Warburg elements were obtained where the electron transport was more dominative under dark conditions. In the case of the pellets, the Nyquist plots for the various ac applied voltages were indistinct and formed into a single semi-circle. We conclude from the above observations that the variation in the observed dielectric phenomenon under illumination could originate from trap-filled ionic transport's domination over electronic transport.

Equivalent Electrical Circuit Analysis. We have performed equivalent circuit modeling for individual Nyquist plots obtained under dark and illumination conditions to reveal insights into the asymmetrical dielectric phenomenon of synthesized $MAPbBr_3$ crystals across their various opposite faces (Figure 5). Since two semi-circles at high frequency (range Hz to 1 kHz) and low frequency (range 10 kHz to MHz) were distinct under dark condition impedance measurements across the opposite faces of crystals and their pellet forms, we have developed the equivalent circuit with two parallel RC circuits. In addition, we have incorporated series resistances in the circuit to represent contact and recombination processes (Figure S2) within crystals. At a low-frequency regime, in the RC circuits for all the opposite faces and pellets, the capacitor was replaced by a constant phase element to fit the circuit with the experimental results better. Under green illumination conditions, the electrical equivalent circuits are different across the three faces of the crystals. Each unique behavior was noted across identical faces of various examined crystals (Figure S4). The variation in the equivalent circuit parameters across the faces of $MAPbBr_3$ crystals and the pellets is summarized in Tables S1−S4. Here, we have observed that the dielectric behavior is different for the various opposite faces of $MAPbBr_3$ crystals, which is also separate from the dielectric nature of the pellets in the powdered form. Furthermore, the dielectric nature of the crystals also varies under illumination due to photogenerated charge carriers. To understand the origin of the change in dielectric behavior across various faces, we have also performed electrical measurements across the opposite faces of multiple faces and powdered pellets.

Electrical Properties. To investigate the asymmetrical dielectric behavior across various faces present in the $MAPbBr_3$ crystals, we have examined the electrical transport properties by measuring current with an applied dc bias across the three opposite faces of multiple crystals under dark and green illumination conditions. Under green illumination conditions, we could observe an increase in current (in the range of μA) across the opposite faces of the crystal (Figure 6) due to photocarrier generation. Furthermore, the measured current values under dark and illumination conditions were higher across the crystal's face III than in the remaining two.

Under the dark conditions, $I-V$ across the opposite faces of the crystals and in pellet form depicted two major regimes due to the limitation of dominant carriers across the various faces of $MAPbBr_3$ crystals (Figure S5). As a result, the ohmic regime is separated from the non-linear current increment regime and saturated at higher applied biases. Considering the SCLC technique, we analyzed the $I-V$ of $MAPbBr_3$ crystals across various faces and powdered pellets to find the parameters from electrical characterization, such as trap density and carrier mobility using the trap-filled limit voltage (V_{TFL}) equation

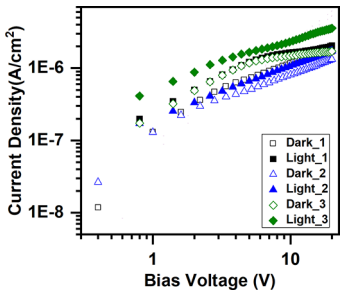

Figure 6. Current−voltage characteristics across the three faces of $MAPbBr_3$ crystals. The numerical numbers represent the opposite faces defined in Figure 1.

$$n_t = \frac{2V_{TFL}\mathcal{E}_0\mathcal{E}_r}{\mathcal{E}L^2} \quad (1)$$

In eq 1, E_0 is the vacuum permittivity, E_r is the relative dielectric constant, and L is the crystal thickness (thickness between opposite faces).[28,29] The trap densities of $MAPbBr_3$ crystals across various opposite surfaces were obtained and are listed in Table 1. The charge carrier mobility in the $MAPbBr_3$ crystal along different face directions was obtained by fitting $I-V$ graphs at higher biases with the Mott−Gurney law in the Child regime.[28] The carrier mobility, along with varying face directions within $MAPbBr_3$ crystals of various surface areas and pellets, was obtained using the equation

$$J_d = \frac{9\mathcal{E}_r\mathcal{E}_0\mu V^2}{8L^3} \quad (2)$$

Here, J_d is the current density, and μ is the mobility of the charge carriers.

We have observed that even face III of the crystal, having a lower electrical contact area and being comparatively larger in thickness, has improved electrical parameter values by an order of magnitude in the calculated electrical mobility and trap density values with lower hysteresis. Furthermore, the dominant electronic transport from impedance spectroscopy studies supports crystal face III's obtained electrical mobility.

These discrepancies in the case of electronic and dielectric properties across various faces of the synthesized $MAPbBr_3$ crystals are due to structural defects, and these could be due to multiple types of defects. For example, density functional theories have been performed on various halide perovskite crystals to understand defects such as Frenkel defects due to the absence of Pb^{2+}, I^-, or MA^+ vacancies, and Schottky pair defects are due to $PbBr_2$ or MAI defects that do not generate trap states.[30−32] Since the current reaches the saturation domain for the more significant path along face III, contradicting the I−V nature across the crystals, we further investigated the correlations between electron transport and structural characterization across the various faces of our synthesized $MAPbBr_3$ crystals.

Structural Characterization. As reported in previous studies, we have studied the structural characterization of the synthesized $MAPbBr_3$ crystals utilizing the powdered X-ray diffraction technique.[10] The diffraction peaks (011), (010), (020), (021), (121), (022), (122), (030), and (031) correspond to the cubic phase of $MAPbBr_3$ crystals and confirm the presence of all the elements of $MAPbBr_3$ crystals.[33] In this study, we examined X-ray diffraction of our synthesized mm-dimension $MAPbBr_3$ crystals on various faces, utilizing a

https://doi.org/10.1021/acsomega.2c04681
ACS Omega 2022, 7, 42138−42145

Table 1. Trap Density and Mobilities of $MAPbBr_3$ Crystals and Powdered Form of Pellets from eq 1 and 2 with Structural Dimensions

	surface area (mm^2)	thickness (mm)	dielectric constant	trap density (cm^3)	mobility ($cm^2\ V^{-1}\ S^{-1}$)
face I	12	2	78.2	1.61×10^9	40.6
face II	8	3	88.3	5.65×10^9	33.42
face III	6	4	112.9	6.54×10^8	225.01
powdered pellet	53.42	1.01	61	4.96×10^{10}	31.7

3D printed adapter on the sample holder of the X-ray diffractometer (Figure 7). We confirmed the presence of the

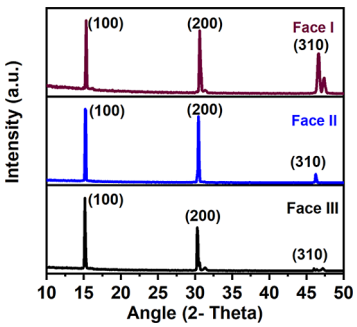

Figure 7. XRD spectra of $MAPbBr_3$ crystals across the three opposite faces.

elements with the peak positions at (100), (200), and (310) planes. Surprisingly, the intensity of the (310) plane varies prominently with the various faces of the crystal, which depict a structural alteration across different faces of synthesized $MAPbBr_3$ crystals.

The presence of the (310) plane across the specific crystal faces (in faces I and II) indicates the unparallel plane that strays the crystals' single-crystalline nature; furthermore, we observe a reduction in the intensity of the (310) plane from face I to face III. The splitting in the planes is due to a phase transition, which was reported as a transition from the cubical nature of the crystals to the tetragonal shape.[34] For face I, the splitting confirms crystal symmetry changes across the various faces. As a result, the synthesized crystals contain cubic and tetragonal phases depending on opposite face directions. Moreover, the (310) plane that is unparallel to the (100) and (200) planes develops grain boundaries across the opposite face I and face II directions, which hinders the directional electronic transport contribution in the presence of trap densities and carriers' recombination at grain boundaries.[35]

On the other hand, the much low-intensity peak of the (310) plane across face III supports a nearly single-crystalline nature, enhancing the electronic transport contributions across the opposite faces of the $MAPbBr_3$ crystals.[21]

Under dark conditions, we have observed that electron transport dominates the ionic contribution across faces II and III of $MAPbBr_3$ crystals (Figure 3b,c). In contrast, the ion transport dominates at a lower frequency regime (20 Hz to 10 kHz) across face I of $MAPbBr_3$ crystals, having a smaller distance between two opposite faces (2 mm in Figure 3a). In addition, we have analyzed the dielectric properties of the crystals using equivalent circuit modeling and observed that because of more negligible recombination resistance and capacitance at a low-frequency regime, the trap densities across face III are low, thus enhancing the carrier mobilities.

Under the green illumination conditions, we have observed that the finite Warburg element is present at the higher frequency regime for face I. Due to the diffusion of photogenerated carriers' current, the ionic contribution is limited, and the dominant transport is under dark conditions. Similarly, in the case of face III at a lower frequency regime, we could observe the Warburg element (mentioned in the earlier section), representing the limitation of electronic transport at that regime due to diffusion of the dominant photogenerated carriers (Figure 4c). Since the unparallel (310) plane is less intense across face III, which resembles single-crystalline nature, we have observed electrical carrier dominance. This is also confirmed by the $I-V$ behavior of the crystals across various plane orientations. Due to the dominant electronic transport across the low intense peak of the unparallel (310) plane, there is an improvement in the electrical parameters such as trap density and carrier mobilities (Table S4). Similarly, for the higher width of the dielectric layer across face III under illumination conditions, the Warburg element is present at a higher frequency regime since generated photocarriers limit the carrier transport, thus enhancing the ionic contribution across the crystals. In the case of the moderate thickness of the dielectric layer, there is the contribution of electron transport and the ionic ones; thus, there is no limitation on carrier transport or ionic motion under illumination conditions due to the generated photo carriers .

$MAPbBr_3$ in pellets contains many grain boundaries, enhancing charge carrier trap densities by an order of magnitude compared to the $MAPbBr_3$ single crystals, which reduced carrier mobilities even with lower dielectric layer thickness. Thus, the required parameters, such as lower trap density and higher carrier mobility, are obtained in the case of single crystals compared to the pellet form of the powdered crystals. Due to the more ion excitation under illumination, the resistance has gained a higher value (10−40 MΩ) across the single crystal compared to the pellet form of the powdered crystals. Thus, under illumination conditions, we could observe more ionic contribution of the elements due to the photogenerated carriers.[36] (Figures 3d,[10] 4d[10] (Reprinted with permission from ref 10 with license number 5351940481677. Copyright 2022 Elsevier)).

From the equivalent model analysis, we could find out the elements present in the system. Under dark conditions, since there is no limit to any photogenerated carriers or ionic mobility, the circuit takes the form of two parallel RC circuits (Figure S2) in which the values of capacitance and resistance are varied with different plane orientations at higher and lower frequency regimes due to the dominant transport carriers according to the various faces listed in Table1. Under illumination conditions, since a limiting factor plays a role based on the dominant transport across multiple faces of the crystals, the equivalent circuits found are different for various plane orientations across the crystal (Figure S3). The corresponding parameters are given in Tables S2−S4.

https://doi.org/10.1021/acsomega.2c04681
ACS Omega 2022, 7, 42138−42145

CONCLUSIONS

In conclusion, we have observed the asymmetric nature of the dielectric behavior across the various faces of the crystals, which affects the electrical nature of the crystals across them. These asymmetric behaviors in the dielectric nature across different plane orientations of the crystals could originate from the dissimilar structural arrangement. The crystals contain cubical and tetragonal characteristics. It could be derived from impurities developed during the synthesis process. Thus, in device fabrication, one can understand the efficacy by understanding the origin of the asymmetric nature. The device performance can improve even with various plane orientations. We also compared the electrical properties of $MAPbBr_3$ single crystals across three faces of different surface dimensional areas and the pellet form of the powdered crystals. We have observed that single crystals have lower trap density and higher carrier mobility than the powdered crystals' pellet form, which is efficient for optoelectronic applications due to the lack of grain boundaries. We have also found much improvement in the electrical parameters across one crystal plane orientation of the crystals justified with impedance analysis. Due to the less ionic contribution at a lower frequency regime across the single crystals, the face, which has a less intense peak of an un-parallel (310) plane in the XRD pattern and is responsible for high carrier mobility, lower trap densities, and high dielectric constant values since it has fewer impurities across it, would thus be more suitable in device performance such as solar cells and photodetectors for efficient electrical contact.

ASSOCIATED CONTENT

Supporting Information

The Supporting Information is available free of charge at https://pubs.acs.org/doi/10.1021/acsomega.2c04681.

> Representation of the synthesis mechanism of $MAPbBr_3$ crystals; dielectric properties; equivalent electrical circuit utilized to analyze experimentally obtained impedance spectra for all the faces of the crystals under dark conditions; equivalent circuit model for all the faces of the crystals under green illumination conditions for faces I, II, and III; fitted curves for Nyquist plots under dark and illumination conditions; electrical properties; equivalent fitting parameters of Nyquist plots for all the faces of $MAPbBr_3$ crystals for ac applied voltages of 50 and 300 mV; equivalent fitting parameters of Nyquist plots across face II of $MAPbBr_3$ crystals and 300 mV under dark conditions; and equivalent fitting parameters of Nyquist plots across face III of $MAPbBr_3$ crystals and 300 mV under green illumination conditions (PDF)

AUTHOR INFORMATION

Corresponding Authors

Dr. Satyajit Gupta − *Department of Chemistry, Indian Institute of Technology, Bhilai 492015, India;* orcid.org/0000-0002-5323-341X; Email: satyajit@iitbhilai.ac.in

Dr. Sabyasachi Mukhopadhyay − *Department of Physics, SRM University—Andhra Pradesh, Andhra Pradesh 522240, India;* orcid.org/0000-0002-6290-6380; Email: sabyasachi.m@srmap.edu.in

Authors

Kunchanapalli Ramya − *Department of Physics, SRM University—Andhra Pradesh, Andhra Pradesh 522240, India*

Arindam Mondal − *Department of Chemistry, Indian Institute of Technology, Bhilai 492015, India*

Complete contact information is available at: https://pubs.acs.org/10.1021/acsomega.2c04681

Notes

The authors declare no competing financial interest.

ACKNOWLEDGMENTS

K.R. acknowledges SRM University AP research funding for her fellowships, and A.M. thanks MoE for the research fellowship. S.G. thanks IIT Bhilai for Research Initiation Grant. In addition, S.M. and S.G. acknowledge the Science and Engineering Research Board, Department of Science and Technology for Early Career Research Award, and Indo-Israeli Joint Research Project (ECR/2017/001937 and DST/INT/ISR/P-28/2020, respectively).

REFERENCES

(1) Lin, C. Stabilizing Organic-Inorganic Lead Halide Perovskite Solar Cells With Efficiency Beyond 20%. *Front. Chem.* **2020**, *8*, 592.

(2) Xu, F.; Zhang, T.; Li, G.; Zhao, Y. Mixed Cation Hybrid Lead Halide Perovskites with Enhanced Performance and Stability. *J. Mater. Chem. A* **2017**, *5*, 11450−11461.

(3) Rosales, B. A.; Hanrahan, M. P.; Boote, B. W.; Rossini, A. J.; Smith, E. A.; Vela, J. Lead Halide Perovskites: Challenges and Opportunities in Advanced Synthesis and Spectroscopy. *ACS Energy Lett.* **2017**, *2*, 906−914.

(4) Miyasaka, T. Lead Halide Perovskites in Thin Film Photovoltaics: Background and Perspectives. *Bull. Chem. Soc. Jpn.* **2018**, *91*, 1058−1068.

(5) Akhtar, J.; Aamir, M.; Sher, M.Organometal Lead Halide Perovskite. In *Perovskite Photovoltaics*; Thomas, S., Thankappan, A., Eds.; Academic Press, 2018, pp 25−42. DOI: 10.1016/B978-0-12-812915-9.00002-2.

(6) Chen, Y.; Liu, S.; Zhou, N.; Li, N.; Zhou, H.; Sun, L.-D.; Yan, C.-H. An Overview of Rare Earth Coupled Lead Halide Perovskite and Its Application in Photovoltaics and Light Emitting Devices. *Prog. Mater. Sci.* **2021**, *120*, 100737.

(7) Shao, Y.; Fang, Y.; Li, T.; Wang, Q.; Dong, Q.; Deng, Y.; Yuan, Y.; Wei, H.; Wang, M.; Gruverman, A.; Shield, J.; Huang, J. Grain boundary dominated ion migration in polycrystalline organic-inorganic halide perovskite films. *Energy Environ. Sci.* **2016**, *9*, 1752−1759.

(8) Park, J.-S.; Walsh, A. Modeling Grain Boundaries in Polycrystalline Halide Perovskite Solar Cells. *Annu. Rev. Condens. Matter Phys.* **2021**, *12*, 95−109.

(9) Zhou, Y.; Padture, N. P.Understanding and Engineering Grain Boundaries for High-Performance Halide Perovskite Photovoltaics. In *2020 47th IEEE Photovoltaic Specialists Conference*; PVSC), 2020, pp 2316−2320. DOI: 10.1109/PVSC45281.2020.9300757.

(10) Ramya, K.; Mondal, A.; Tyagi, M.; Gupta, S.; Mukhopadhyay, S. Room-Temperature Cost-Effective in-Situ Grown MAPbBr3 Crystals and Their Characterization towards Optoelectronic Devices. *Mater. Sci. Eng., B* **2022**, *283*, 115840.

(11) Dang, Y.; Ju, D.; Wang, L.; Tao, X. Recent Progress in the Synthesis of Hybrid Halide Perovskite Single Crystals. *CrystEngComm* **2016**, *18*, 4476−4484.

(12) Di, J.; Chang, J.; Liu, S.; Frank. Recent progress of two-dimensional lead halide perovskite single crystals: Crystal growth, physical properties, and device applications. *EcoMat* **2020**, *2*, No. e12036.

(13) Feng, A.; Jiang, X.; Zhang, X.; Zheng, X.; Zheng, W.; Mohammed, O. F.; Chen, Z.; Bakr, O. M. Shape Control of Metal Halide Perovskite Single Crystals: From Bulk to Nanoscale. *Chem. Mater.* **2020**, *32*, 7602−7617.
(14) Zhang, Y.; Lyu, M.; Qiu, T.; Han, E.; Kim, I. K.; Jung, M.-C.; Ng, Y. H.; Yun, J.-H.; Wang, L.Halide Perovskite Single Crystals: Optoelectronic Applications and Strategical Approaches. *Energies***2020**, *13*(). DOI: 10.3390/en13164250.
(15) Wang, W.; Su, J.; Zhang, L.; Lei, Y.; Wang, D.; Lu, D.; Bai, Y. Growth of Mixed-Halide Perovskite Single Crystals. *CrystEngComm* **2018**, *20*, 1635−1643.
(16) Liu, Y.; Zhang, Y.; Zhu, X.; Feng, J.; Spanopoulos, I.; Ke, W.; He, Y.; Ren, X.; Yang, Z.; Xiao, F.; Zhao, K.; Kanatzidis, M.; Liu, S.; Frank. Triple-Cation and Mixed-Halide Perovskite Single Crystal for High-Performance X-ray Imaging. *Adv. Mater.* **2021**, *33*, 2006010.
(17) Ding, J.; Yan, Q. Progress in Organic-Inorganic Hybrid Halide Perovskite Single Crystal: Growth Techniques and Applications. *Sci. China Mater.* **2017**, *60*, 1063−1078.
(18) Shamsi, J.; Abdelhady, A. L.; Accornero, S.; Arciniegas, M.; Goldoni, L.; Kandada, A. R. S.; Petrozza, A.; Manna, L. N-Methylformamide as a Source of Methylammonium Ions in the Synthesis of Lead Halide Perovskite Nanocrystals and Bulk Crystals. *ACS Energy Lett.* **2016**, *1*, 1042−1048.
(19) Whitfield, P. S.; Herron, N.; Guise, W. E.; Page, K.; Cheng, Y. Q.; Milas, I.; Crawford, M. K. Structures, Phase Transitions and Tricritical Behavior of the Hybrid Perovskite Methyl Ammonium Lead Iodide. *Sci. Rep.* **2016**, *6*, 35685.
(20) Wang, Y.; Lü, X.; Yang, W.; Wen, T.; Yang, L.; Ren, X.; Wang, L.; Lin, Z.; Zhao, Y. Pressure-Induced Phase Transformation, Reversible Amorphization, and Anomalous Visible Light Response in Organolead Bromide Perovskite. *J. Am. Chem. Soc.* **2015**, *137*, 11144−11149.
(21) Chen, L.-C.; Lee, K.-L.; Lin, S.-E.Observation of Hybrid MAPbBr3 Perovskite Bulk Crystals Grown by Repeated Crystallizations. *Crystals***2018**, *8*(). DOI: 10.3390/cryst8070260.
(22) Zuo, Z.; Ding, J.; Zhao, Y.; Du, S.; Li, Y.; Zhan, X.; Cui, H. Enhanced Optoelectronic Performance on the (110) Lattice Plane of an MAPbBr3 Single Crystal. *J. Phys. Chem. Lett.* **2017**, *8*, 684−689.
(23) Lee, J.-W.; Seo, S.; Nandi, P.; Jung, H. S.; Park, N.-G.; Shin, H. Dynamic Structural Property of Organic-Inorganic Metal Halide Perovskite. *iScience* **2021**, *24*, 101959.
(24) Cheng, X.; Jing, L.; Zhao, Y.; Du, S.; Ding, J.; Zhou, T. Crystal Orientation-Dependent Optoelectronic Properties of MAPbCl3 Single Crystals. *J. Mater. Chem. C* **2018**, *6*, 1579−1586.
(25) Cho, Y.; Jung, H. R.; Kim, Y. S.; Kim, Y.; Park, J.; Yoon, S.; Lee, Y.; Cheon, M.; Jeong, S.; Jo, W. High Speed Growth of MAPbBr3 Single Crystals via Low-Temperature Inverting Solubility: Enhancement of Mobility and Trap Density for Photodetector Applications. *Nanoscale* **2021**, *13*, 8275−8282.
(26) Contreras-Bernal, L.; Ramos-Terrón, S.; Riquelme, A.; Boix, P. P.; Idígoras, J.; Mora-Seró, I.; Anta, J. A. Impedance Analysis of Perovskite Solar Cells: A Case Study. *J. Mater. Chem. A* **2019**, *7*, 12191−12200.
(27) Romero, B.; del Pozo, G.; Arredondo Conchillo, B.; Martín-Martín, D.; Hernández-Balaguera, E.; López-González, M. d. C.Characterization of organic and perovskite solar cells by impedance spectroscopy. **2019**; *11095*, 110950N. DOI: 10.1117/12.2530568.
(28) Fru, J. N.; Nombona, N.; Diale, M. Characterization of Thin MAPb(I1-xBrx)3 Alloy Halide Perovskite Films Prepared by Sequential Physical Vapor Deposition. *Front. Energy Res.* **2021**, *9*, 196.
(29) Dacuña, J.; Salleo, A. Modeling Space-Charge-Limited Currents in Organic Semiconductors: Extracting Trap Density and Mobility. *Phys. Rev. B: Condens. Matter Mater. Phys.* **2011**, *84*, 195209.
(30) Parikh, N.; Pandey, M.; Prochowicz, D.; Kalam, A.; Tavakoli, M. M.; Satapathi, S.; Akin, S.; Yadav, P. Investigation on the Facet-Dependent Anisotropy in Halide Perovskite Single Crystals. *J. Phys. Chem. C* **2022**, *126*, 8906−8912.
(31) Kim, D.; Yun, J.-H.; Lyu, M.; Kim, J.; Lim, S.; Yun, J. S.; Wang, L.; Seidel, J. Probing Facet-Dependent Surface Defects in MAPbI3 Perovskite Single Crystals. *J. Phys. Chem. C* **2019**, *123*, 14144−14151.
(32) Ono, L. K.; Liu, S.; Qi, Y. Reducing Detrimental Defects for High-Performance Metal Halide Perovskite Solar Cells. *Angew. Chem., Int. Ed.* **2020**, *59*, 6676−6698.
(33) Tress, W. Metal Halide Perovskites as Mixed Electronic-Ionic Conductors: Challenges and Opportunities-From Hysteresis to Memristivity. *J. Phys. Chem. Lett.* **2017**, *8*, 3106−3114.
(34) Mashiyama, H.; Kawamura, Y.; Magome, E.; Kubota, Y. Displacive Character of the Cubic-Tetragonal Transition in CH3NH3PbX3. *J. Korean Phys. Soc.* **2003**, *42*, S1026−S1029.
(35) Lian, Z.; Yan, Q.; Gao, T.; Ding, J.; Lv, Q.; Ning, C.; Li, Q.; Sun, J. Perovskite CH3NH3PbI3(Cl) Single Crystals: Rapid Solution Growth, Unparalleled Crystalline Quality, and Low Trap Density toward 108 cm-3. *J. Am. Chem. Soc.* **2016**, *138*, 9409−9412.
(36) Smith, E. C.; Ellis, C. L. C.; Javaid, H.; Renna, L. A.; Liu, Y.; Russell, T. P.; Bag, M.; Venkataraman, D. Interplay between Ion Transport, Applied Bias, and Degradation under Illumination in Hybrid Perovskite p-i-n Devices. *J. Phys. Chem. C* **2018**, *122*, 13986−13994.

https://doi.org/10.1021/acsomega.2c04681
ACS Omega 2022, 7, 42138−42145